Dissecting Abdominal Aortic Aneurysm in Ang II-infused Mice: Suprarenal Branch Ruptures and Apparent Luminal Dilatation

Bram Trachet[1,2], Rodrigo A. Fraga-Silva[2], Alessandra Piersigilli[3,4], Alain Tedgui[5], Jessica Sordet-Dessimoz[6], Alberto Astolfo[7], Carole Van der Donckt[8], Peter Modregger[7,9], Marco F.M. Stampanoni[7,10], Patrick Segers[1], Nikolaos Stergiopulos[2]

[1] IBiTech - bioMMeda, Ghent University-iMinds Medical IT, Ghent, Belgium

[2] Institute of Bioengineering, Ecole Polytechnique Fédérale de Lausanne, Lausanne, Switzerland

[3] School of Life Sciences, PTEC GE, Ecole Polytechnique Fédérale de Lausanne, Lausanne, Switzerland

[4] Institute of Animal Pathology, University of Bern, Bern, Switzerland

[5] INSERM, Paris Cardiovascular Research Center (PARCC), Université Paris Descartes, Paris, France

[6] Histology Core Facility, Ecole Polytechnique Fédérale de Lausanne, Lausanne, Switzerland

[7] Swiss Light Source, Paul Scherrer Institut, Villigen, Switzerland

[8] Laboratory of Physiopharmacology, University of Antwerp, Antwerp, Belgium

[9] Centre d'Imagerie BioMédicale, Ecole Polytechnique Fédérale de Lausanne, Switzerland

[10] Institute for Biomedical Engineering, University and ETH Zürich, Zürich, Switzerland

Bram Trachet

LHTC STI IBI EPFL
BM 5128 Station 17
CH-1015 Lausanne (Switzerland)
Tel: +41 21 693 83 81
Fax: +41 21 693 96 35

bram.trachet@ugent.be

Dissecting Abdominal Aortic Aneurysm in Ang II-infused Mice: Suprarenal Branch Ruptures and Apparent Luminal Dilatation

Bram Trachet; Rodrigo A. Fraga-Silva; Alessandra Piersigilli; Alain Tedgui; Jessica Sordet-Dessimoz; Alberto Astolfo; Carole Van der Donckt; Peter Modregger; Marco F.M. Stampanoni; Patrick Segers; Nikolaos Stergiopulos

Cardiovascular Research 2014

doi: 10.1093/cvr/cvu257

Abstract

Aims

In this work we provide novel insight into the morphology of dissecting abdominal aortic aneurysms in angiotensin II-infused mice. We demonstrate why they exhibit a large variation in shape and, unlike their human counterparts, are located suprarenally rather than infrarenally.

Methods and Results

We combined synchrotron-based ultra-high resolution ex vivo imaging (phase contrast X-Ray tomographic microscopy) with in vivo imaging (high-frequency ultrasound and contrast-enhanced micro-CT) and image-guided histology. In all mice we observed a tear in the tunica media of the abdominal aorta near the ostium of the celiac artery. Independently we found that, unlike the gradual luminal expansion typical for human aneurysms, the outer diameter increase of angiotensin II-induced dissecting aneurysms in mice was related to one or several intramural hematomas. These were caused by ruptures of the tunica media near the ostium of small suprarenal side branches, which had never been detected by the established small-animal imaging techniques. The tear near the celiac artery led to apparent luminal dilatation, while the intramural hematoma led to a dissection of the tunica adventitia on the left suprarenal side of the aorta. The number of ruptured branches was higher in those aneurysms that extended into the thoracic aorta, which explained the observed variability in aneurysm shape.

Conclusions

Our results are the first to describe apparent luminal dilatation, suprarenal branch ruptures and intramural hematoma formation in dissecting abdominal aortic aneurysms in mice. Moreover we validate and demonstrate the vast potential of phase contrast X-Ray tomographic microscopy in cardiovascular small animal applications.

Keywords

Abdominal aortic aneurysm, X-ray computed tomography, grating interferometry, angiotensin II, mouse model

Introduction

Abdominal aortic aneurysm (AAA) occurs in 5 to 9% of the population over the age of 65 years [1] and transmural aneurysm rupture is the 10th cause of death in the industrialized world [2]. AAA can be induced by the infusion of angiotensin II in hypercholesterolemic mice [3-6], which leads to relatively stable AAA [7], or by a combined infusion of angiotensin II and anti-TGF-β antibodies in normolipidemic mice [8], which leads to more rupture-prone AAA [9]. Angiotensin II-infused mice form the basis of most preclinical pharmacological aneurysm research [10-15]. According to literature, the early phase of angiotensin-II infusion is characterized by macrophage infiltration, medial elastolysis, luminal expansion and thrombus formation [3, 4, 6, 7]. All these characteristics are also present in human AAA[16], yet important patho-morphological differences exist between mice and men[17]. In mice, the AAA (i) develops suprarenally rather than infrarenally [3, 5], (ii) shows sudden rather than slowly progressing luminal dilatation [4, 6] and (iii) presents intramural rather than intraluminal thrombus [18]. For this reason, in the current manuscript the term 'dissecting AAA'[18] was preferred over the more commonly used 'AAA'. A large variability within murine dissecting AAA shapes has been reported, classified from grade I (dilated suprarenal lumen without thrombus) over grade II and III (remodeled tissue with/without thrombus, often located eccentrically on the left side of the suprarenal aorta) to grade IV (polymorphic AAA with multiple aneurysms along the suprarenal and thoracic aorta) [5, 12]. These morphological differences have been reported by different laboratories and in different mouse models, but have never been fully explained. We hypothesized that better imaging techniques, visualizing the aortic wall at an ultra-high resolution and in 3D, might allow us to understand which processes lead to the macroscopically observed phenomena.

An accurate morphologic evaluation at microscopic level can be achieved through histopathology, but this relies on 2-dimensional sections which makes 3D reconstruction and analysis challenging if not impossible[18]. In vitro (vascular casting) as well as in vivo (contrast-enhanced) micro-CT offer an isotropic pixel size up to 50 μm, but are restricted to the blood-filled aortic lumen and do not allow for visualization of the aortic wall [19]. In vivo micro-MRI provides soft tissue contrast visualizing the aortic wall but the typical through-plane distance is too coarse (order of magnitude 100-200 μm) for detailed 3D analyses [9, 20, 21]. Finally, 3D ultrasound offers a detailed in-plane pixel size (up to 15 μm) and through-plane distance (up to 35 μm) as well as limited soft tissue contrast, but it is a highly operator-dependent technique that is often subject to interpretation [22]. Differential phase contrast X-Ray tomographic microscopy (PCXTM) uses synchrotron radiation to overcome all these limitations as it combines detailed soft tissue contrast (obtained through grating interferometry) with an isotropic pixel size of 6.5 μm [23, 24].

In this work, we validated PCXTM with PCXTM-guided histology to obtain a detailed insight into the global 3D morphology at specific locations of interest along dissecting AAAs. Combining these novel ultra-high resolution imaging techniques with in vivo imaging (ultrasound and micro-CT), we provide novel insight into the mechanism behind dissecting AAA formation, induced by combined angiotensin II infusion and anti-TGF-β antibody injection in C57BL/6J mice.

Methods

Sample size.

20 manipulated animals and 5 controls were included in the in vivo imaging part of the study. Two animals died from other causes than transmural aneurysm rupture (found dead in the cage without hemoabdomen) and 3 animals did not respond to the treatment and did not develop any dissecting AAA. The priority criterion for PCXTM imaging was the macroscopic evidence of dissecting AAA after excision. A total of 20 animals (15 dissecting AAAs, 4 controls and 1 non-responder) were imaged with PCXTM. Since the aim of the study was to describe the morphology of dissecting AAAs and not to compare a pre-defined effect in different groups, there was no group allocation within the aneurysmatic animals prior to data analysis. There were two experimental groups (dissecting AAAs and controls) and aneurysmatic animals were classified into different categories a posteriori based on morphological characteristics observed on the PCXTM scans. Subsequently there was no need for randomization of the data or blinding during data analysis.

In vivo experiments

All the procedures were approved by the Ethical Committee of Canton Vaud, Switzerland (EC 2647.1) and performed according to the guidelines from Directive 2010/63/EU of the European Parliament on the protection of animals used for scientific purposes. Male C57BL/6J male mice were purchased at the age of 12 weeks from Janvier (Saint Berthevin, France). All manipulated mice (n=20) were implanted a 200 µl osmotic pump (model Alzet 2004; Durect Corp, Cupertino, CA), filled with a solution of angiotensin II (Bachem, Bubendorf, Switzerland). Systemic neutralization of TGF-β was achieved by intraperitoneal injections of mouse anti–human TGF-β (2G7 clone, 20 mg/kg, three times a week). Dissecting AAA progression was longitudinally monitored at different time points in vivo using high-frequency ultrasound (Vevo 2100, VisualSonics, Toronto, Canada). Before sacrifice, 6 animals with obvious dissecting AAA presence (as confirmed on ultrasound) were injected intravenously in the lateral tail vein with 4 µl/gram body weight of ExiTron nano 12000 (Miltenyi Biotec, Bergisch Gladbach, Germany). These animals were subsequently scanned in vivo with a Quantum FX micro-CT scanner (Caliper Life Sciences, Hopkinton, Massachusets). During both ultrasound and micro-CT imaging animals were anesthetized by inhalation of 1.5% isoflurane. At the endpoints of the experiments, the mice were anesthetized by Ketamine/Xylazine (100 mg/kg and 15 mg/kg, respectively) and the sacrifice was resolved following the tissue collection.

Ex vivo experiments

After sacrifice, the aorta was flushed in situ by transcardiac perfusion of phosphate buffered saline (PBS, pH 7.4) through the left ventricle. In animals that died of transmural rupture of the aneurysmatic wall, the aorta was collected (without flushing) as soon as possible after finding them in the cage. The abdominal aorta of both intact and transmurally ruptured dissecting AAAs was carefully excised and samples were fixed by immersion in 4% paraformaldehyde (PFA) in 0.15 mM PBS. The samples were scanned at the TOMCAT beamline of the Swiss Light Source, Paul Scherrer Institut, Villigen, Switzerland. All reconstructed datasets (in vivo as well as PCXTM) were semi-automatically segmented into 3D models using the commercial software package Mimics (Materialise, Leuven, Belgium). After PCXTM scanning, the samples were

fixed as mentioned above, processed and embedded in paraffin according to standard histological procedures. 4 µm thick paraffin sections were carefully compared to the corresponding PCXTM images under a Leica DM750 bright field microscope to spot the exact rupture sites.

A more detailed description of the methods can be found in the supplementary materials.

Results

PCXTM - morphological imaging We observed that two different phenomena led to the formation of an AAA-like geometry in angiotensin II-infused mice.

A first observation, invariably occurring in all aneurysmatic mice (15/15), was a mural tear of the tunica media that originated in the suprarenal segment near the ostium of the celiac artery. The medial tear ran in cranio-caudal direction over an average axial distance of 1.8 ± 1.1 mm. It was located either on the left side (6/15, Fig. 1*c*, 3*c*), or on the ventral side of the aorta (9/15, Fig. 2*c*, 4*c* and 5*d*). Tears on the left side extended from the cranial to the caudal side of the ostium of the celiac branch (Fig. 1*c*, 3*c*). Those on the ventral side of the aorta were most often located caudally to the ostium of the celiac branch (6/15, Fig. 2*c*, 5*d*), but they could also occur cranially (1/15) or extend both caudally and cranially (2/15, Fig. 4*c*).

A second observation, occurring in the majority of aneurysmatic mice (13/15), was a local destruction and rupture of the medial architecture near the ostium of one or several small abdominal side branches. One to six ruptured branches were counted per specimen and the affected branches were located either on the left (84% of all ruptured branches) or the dorsal side (16%) of the aorta. Almost all ruptures occurred in branches located cranially to the celiac artery (94%). Affected branches included the superior suprarenal artery, supplying blood to the left adrenal gland, as well as various small abdominal branches and the most caudal of the intercostal arteries. Each of these mural ruptures led to an intramural hematoma dissecting the tunica media from the adventitia. Flow lines of alternated layers of blood cells and fibrin (Zahn's lines) were clearly discernible on the PCXTM images as alternating concentric layers around the vascular breach (Fig. 3*a*, 5*g*).

PCXTM – rupture site imaging In 6 animals which were scanned in vivo using contrast-enhanced micro-CT two hours prior to sacrifice and aorta collection, the contrast agent (ExiTron) could be visualized on the PCXTM images as dense white aggregates. Due to the small size of the particles (diameter 0.11 μm), and to the discontinuity of the intimal and medial layers, Exitron entered the aortic wall together with erythrocytes (diameter 6-7 μm) along the edges of the tear in the tunica media near the celiac artery and near the ruptured ostium of suprarenal and other abdominal side branches (Fig. 2*a*, 4*e*). Moreover, ExiTron also percolated into the tunica media near the ostia of intact intercostal arteries and abdominal side branches (2 to 10 affected branch ostia per specimen). Since the aortas were flushed after sacrifice, these areas indicate intra vitam local increased permeability of the vessel due to disruption of the wall, with loss of the layered architecture (Fig. 2*b*, top). The CD-31 stain showed focal hypertrophy of endothelium (endothelial activation), and the Hematoxylin and Eosin (H&E) stain showed widening of intercellular spaces and mild to moderate segmental thickening of the intima, due to accumulation of Exitron, single apoptotic cells and erythrocytes. Single erythrocytes (focal microhemorrhages) and cellular debris were seen within the tunica media, while the adventitia was moderately infiltrated by leukocytes (Fig. 2*b*, top).

Dissecting AAA initiation, progression and rupture. The two main events influencing the final morphology were: (i) the number of ruptured side branches and (ii) the location of the tear in the tunica media with respect to the intramural hematoma. The number of ruptured branches determined whether the intramural hematoma was either non-existent, limited to the abdominal

aorta, or extended into the thoracic aorta. The interaction between the tear in the tunica media and the location of the dissected adventitia determined whether a so-called 'false channel' was formed or not. We chose to describe five different cases that illustrate how the interaction between the intramural hematoma and the medial tear influenced the final morphology of the dissecting AAAs.

Case 1: medial tear but no intramural hematoma, dissecting AAA restricted to the abdominal region

In a limited amount of samples, the tear in the tunica intima and media near the celiac artery was the only observed lesion: supraceliac side branches remained intact (2/15, Fig. 1). Along the tear, degeneration and rupture of elastic lamellae (Fig 1B top) and smooth muscle cells (Fig 1D bottom) occurred. The tear was covered by aggregated platelets and polymerized fibrinogen (fibrin) forming an hemostatic clot (Fig. 1*d*). This was sufficient to avoid further leakage from the lumen and later on provided a scaffold for migration of endothelial cells to re-endothelialize the denudated vessel. Rapid blood flow in arteries and arterioles limited passive incorporation of erythrocytes within the plug [25]. Since no rupture of the superior suprarenal artery or any other abdominal branches occurred, the medial tear just led to a small suprarenal segmental expansion of the arterial wall without any intramural hematoma formation. This lesion would previously have been categorized as a Grade I aneurysm.

Case 2: medial tear and intramural hematoma without false channel formation, dissecting AAA restricted to the abdominal region

In most cases (13/15), the tear in the tunica intima and media near the celiac artery co-existed with the rupture of one or several small suprarenal abdominal branches. In 3/15 cases the intramural hematoma was limited to the abdominal aorta while the tear in the tunica media was located on the ventral side of the aorta and caudally to the celiac artery (Fig.2). Since the intramural hematoma was occurring more cranially and leftwards, the adventitia was focally dissected from the media due to the hematoma while it remained intact in the area adjacent to the celiac tear (Fig. 2*b bottom*). In this case, the intramural hematoma and the tear in the tunica media were two separate, independent events. Since the bleeding was focal, and no false channel was formed, it resulted in intramural blood accumulation. At the site of rupture clotted blood was present (Fig. 2*d top*) and 9 days after the event, progressive fibrin organization, spindle cells migration and angiogenesis were evident and proceeded mostly in a centrifugal manner from the lumen (Fig. 2*e*, top and middle). Hemosiderophages at the periphery of the hematoma (highlighted with Prussian Blue histochemical stain for iron, Fig. 2*e* bottom) accounted for ongoing hematoma resorption. ExiTron particles that infiltrated the wall exhibited a typical grey-greenish discoloration of phagocytic cells [26] on the H&E stain (Fig. 2*e* top). Over time collagen was deposited (most likely by migrating smooth muscle cells, myofibroblasts and adventitial fibroblasts) at the rupture and hematoma sites (Fig. *2b*, 4*d*). These data support the contributing role of newly synthesized collagen to an intramural wound-healing response described earlier by Schriefl et al [18].

Cases 3 - 4: medial tear and intramural hematoma with false channel formation, dissecting AAA restricted to the abdominal region

In 3/15 cases, the intramural hematoma was limited to the abdominal aorta and the dissected adventitia surrounded the tear in the tunica media (Fig. 3, 4). Depending on the amount of thrombus that was externally visible, these animals would previously have been categorized as Grade II or Grade III aneurysms. In one animal that was sacrificed 2 days after first detection of the dissecting AAA, a large tear in the tunica media ran on the left side of the celiac artery, extending both cranially and caudally of the latter (Fig. 3). Along the length of the tear, blood flew out of the original lumen profile forming a large, focal apparent dilatation (Fig 3*a*, 3*c*). The hemostatic plug layering the dilated lumen was surrounded by clotted blood (Fig. 3*b*). The latter was walled off by the adventitia, which had been dissected by the mural rupture of the tunica media near the ostium of the superior suprarenal artery (Fig 3*b*, top). The dilated lumen extended cranially into the hematoma, thus forming a false channel parallel to the original lumen (Fig 3*b*, middle). The dissection of the adventitia was stopped at the cranial end by a small branch that acted as a physical anchor point, inhibiting further peeling off of the adventitial layer (Fig *3c*). The caudal aspect of the proximal segment of this branch was infiltrated by inflammatory cells (neutrophils and phagocytes), causing elastolysis and medial degeneration (Fig. 3*d*, top).

In another animal that was sacrificed 10 days after first detection of a dissecting AAA on ultrasound, a small tear in the tunica media was located on the left side of the aorta, cranially to the celiac artery (Fig. 4). In this case blood was no longer flowing out of the "real" lumen of the ruptured superior suprarenal artery as the small false lumen that was visible at this location in the younger dissecting AAA (Fig. *3b top*) had been filled with fibrin and platelets (Fig. *4d top*). Consecutive 3D ultrasound showed in vivo how another false channel formed near the celiac artery over the course of several days (Fig. 4*a*). The presence of free flowing blood in this false channel (but not in the more cranial part of the intramural hematoma) was confirmed by contrast-enhanced in vivo micro-CT, and by Color Doppler images showing a counter-directional vortex forming with blood flowing in cranial direction (Fig. 4*b*). The false channel was much smaller than the one in Fig. 3 and was restricted to the supraceliac region. Its borders were clearly delineated by endothelial cells that had migrated from the rupture site to re-endothelialize the surface of the plug, reducing its thrombogenicity (Fig. *4d middle*). The fibrin layer lining the false channel had become thinner, likely under the modeling effect of local blood flow forces (Figure not shown).

Case 5: medial tear and intramural hematoma without false channel formation, dissecting AAA extending into the thoracic aorta

In 7/15 cases the dissecting AAA was not restricted to the abdominal aorta but had a polymorphic shape that included the thoracic aorta (Fig. 5). These were previously categorized as Grade IV aneurysms The polymorphic shape was directly related to the intramural rupture of additional branches. In total 22 branch ruptured leading to intramural hematomas (with a maximum value of 6 per specimen) were counted on the PCXTM images in these dissecting AAAs, while only 12 ruptured branches (with a maximum value of 3 per specimen) were counted in the dissecting AAAs that were restricted to the abdominal aorta (8/15). Ruptured branches included small abdominal branches cranial to the celiac artery (such as the superior suprarenal artery, Fig. 5*c*) and intercostal arteries (Fig. 5*g top*). For none of the 3 cases depicted in Fig. 5, a dissecting AAA was visible in vivo 2 days before sacrifice. Abdominal 3D ultrasound (Fig. 5*a*), Color Doppler

297 (Fig. 5*a*, *5b*) and micro-CT measurements (Fig. 5*c*) confirmed there was no false channel
298 formation, except for a small false lumen at the level of the ruptured superior suprarenal artery
299 that could be observed on micro-CT (Fig. 5*c*). The compression of the adventitia on its inner side,
300 exerted by the large hematoma, caused separation of collagen fibers with multifocal loss of
301 continuity of the layer and leakage of blood (Fig. 5*e*) outside the vessel and into the abdomen
302 (hemoabdomen).

303

304 ***Case 6: Transmural rupture***

305 Dissecting AAA transmural rupture occurred most often in dissecting AAAs extending into the
306 thoracic aorta (5/6 lethal dissecting AAAs had a thoracic part, Fig. 6). None of them could be
307 imaged before transmural rupture had occurred (6/6 were found dead presenting internal
308 bleeding). In the depicted case, the tear in the tunica media had propagated further cranially,
309 connecting to the ostium of the ruptured superior suprarenal branch, which is clearly visible on
310 the combined Miller and Sirius Red stain (Fig. 6*b*, middle). The resulting hemorrhage led to a
311 large intramural hematoma caudally to the tear near the celiac artery (Fig. *6a*, *6b* bottom, 6*c*).
312 Multifocal disruption of the adventitia and perivascular soft tissues led to extravasation of blood
313 into the abdominal space (Fig. 6*b*, box) and most likely caused death of the animal by
314 hemoabdomen.

315

Discussion

The possibility to image with soft tissue contrast at an isotropic pixel size of 6.5 µm makes PCXTM a powerful tool in preclinical cardiovascular research. Moreover the validation of the grayscale images with PCXTM-guided histology (e.g. Fig. 2*a*, 2*b*) allows for a much higher precision than what traditional, non-guided histology can offer. The exact location of rupture near the small branches (Fig. 2*b*middle, 3*b top*, 4*d top* and 6*b middle*), which had never been spotted with existing imaging techniques, could be cut and selected (before staining). Additionally, the 3D representation greatly facilitates the *a posteriori* interpretation of the 2D histological images. We have combined PCXTM-guided histology with in vivo imaging to visualize the mechanism behind pathogenesis and rupture of dissecting AAA in angiotensin II-infused mice. Despite the relatively small sample size, our data are the first to describe the large variation in morphology of these dissecting AAAs in an unequivocal way.

Hypothesis on dissecting AAA pathophysiology

Our data reveal an important role for small aortic branches on both initiation and expansion of dissecting AAAs. Mural ruptures near side branches are preceded by microscopic ruptures of elastic lamellae at branch ostia, as visualized by infiltrated ExiTron particles near the ostia of intact branches. These data confirm the results of Gavish et al [27], who performed serial histology in angiotensin II-infused ApoE $^{-/-}$ mice to show that macrophage infiltration and transmedial breaks occur near the ostia of large abdominal side branches (celiac, mesenteric, and renals). A possible explanation for the important role of small branches lies in the typical flow patterns near the branch ostia, where zones of flow recirculation create local areas of low shear stress [19, 28, 29]. This might lead to endothelial dysfunction with or without denudation, followed by increased binding and eventually transmigration of marginalized leukocytes. As in the pathogenesis of atherosclerosis, hyperlipidemia (and especially hypercholesterolemia) might lead to intimal accumulation of lipoproteins, which in turn could be oxidized and exert a pro-inflammatory, chemo-attractant action on monocytes/macrophages [30, 31]. Moreover, the abrupt change in the number of medial lamellae from the larger aorta to the smaller side branch may induce a locally different reaction to these hemodynamic forces [27, 32], and the mechanical tension exerted by the branch on the tunica media is locally increased at the point of attachment [33].

The upstream formation of a false channel into a previously existing hematoma over the course of several days (Fig. 4) is confirmed when re-interpreting previously published transversal micro-MRI images [21], and is even more pronounced after CNA-35 injection to enhance collagen visibility [9]. It is also confirmed by previously published Color Doppler data, both in the presence [8, 9] or absence [4, 22] of anti-TGF-β blockade. We hypothesize that false channel formation (Fig 3, 4) is related to the fact that in these animals the adventitia (which initially protected the hemostatic plug as in Fig. 1, 2) was dissected by the intramural hematoma. The plug was thus subjected to an intramural pressure difference between the high (arterial) pressure on its luminal side and the low pressure on its outside, exerted by the hematoma. If the fibrin and platelets mesh layer could resist to the initial sudden pressure difference by virtue of its elasticity, they remodeled and were pushed in cranial direction towards the hematoma, thus forming a false channel (Fig. 3*c, 4*c). On the other hand, if the hemostatic plug could not withstand the luminal pressure, blood flowed from the arterial lumen into the hematoma with a much higher volume than what was the case in hematomas caused by mural ruptures near small suprarenal branches. This increased the severity,

hence the size of the hematoma with a significant stress on the adventitial layer causing the latter to rupture (Fig. 6*b,* 6*c*). This hypothesis also implies that the tear in the tunica media near the celiac artery preceded the ruptures at the lumen of small suprarenal branches, which is supported by the existence of dissecting AAAs with a tear and hemostatic plug, but without intramural thrombus (Fig. 1).

A paradigm shift? Comparison with literature

At first sight our data seem to contradict the existing paradigm in AAA research in mice: luminal expansion has been observed or implicitly supported in many papers, while suprarenal branch ruptures have not. However, when taking a closer look at the actual figures in literature on which the existing paradigm has been built, none of them contradict and most of them explicitly support our novel observations and interpretations.

An increase in luminal AAA diameter is usually based on quantification of transversal B-Mode ultrasound images, taken at the level of the 'maximal diameter'[13, 15, 32, 34-38]. Most papers do not show any of the B-Mode images that were used for diameter quantification [13, 15, 32], but the available images can be categorized into two different types: some clearly demonstrate a concentric dilatation of the aortic diameter [36-38], while others visualize an asymmetric distribution of two distinct regions within the circular cross-section [34, 35, 39]. Both types were reproduced by our B-Mode ultrasound. In those cases where B-Mode and Color Doppler images showed an almost concentric, blood-filled, dilated aorta (Figure 3*d* bottom, 4*b* bottom), PCXTM and PCXTM-guided histology invariably showed a tear in the tunica media (Fig. 3*a bottom*, 3*b bottom*, 4*d bottom*, 4*e bottom*). This was confirmed by a vast amount of literature: wherever a luminal expansion is visible on histology, it coincides with a tear in the tunica media [3-9, 18, 27, 29, 32, 34, 36, 37].

At most locations, however, the cross-section on our B-Mode images was partly filled by a grey, speckled (Fig. 3*d* middle) or sometimes black (Fig 5*b* top) region, similar to what had been reported before [34, 35]. Color Doppler revealed that at these locations blood flow remained within the original aortic lumen (Fig. 3*d* middle, 4*b* middle, 5*b*), which was confirmed in vivo by contrast-enhanced micro-CT (Fig. 4*b*, 5*c*). At these regions PCXTM and PCXTM-guided histology invariably showed a non-dilated lumen in an intact, tunica adjacent to an intramural hematoma (Fig. 2*b* bottom, 3*b* top, 4*d* top, 5*e* top). We therefore speculate that the diameter value that was used to quantify 'luminal expansion' with ultrasound should in most cases be re-interpreted as an expansion of the outer wall of the tunica adventitia due to formation of an intramural hematoma. The lack of true luminal dilatation in some of the dissecting AAAs has been confirmed by in vivo micro-CT [19, 29] and MRI [21, 40-42], and almost all papers include histology images of an intact aortic media adjacent to an intramural region [3-9, 18, 27-29, 31-34]. The only difference is that in these cases the intramural region was often termed a 'remodeled adventitia' or 'thrombus' and when it was termed a hematoma, its source was not identified. We are the first to relate the intramural hematoma to additional ruptures of suprarenal branches.

Limitations and conclusions

At this stage, our observations are limited to C57BL/6J mice undergoing simultaneous angiotensin II infusion and systemic neutralization of TGF-β. These mice have been reported to have a higher incidence of grade IV, polymorphic AAAs and to succumb more often due to transmural dissecting AAA rupture than the more commonly used angiotensin II-infused ApoE $^{-/-}$ mice [8]. This explains why in the current study animals were sacrificed at a relatively early stage of dissecting AAA formation, and why 7 out of the 15 observed dissecting AAAs extended into the thoracic aorta. Despite the fact that literature data (from histology [4, 18, 27], ultrasound [34, 35, 39], micro-CT [19, 29] and MRI [21, 40-42]) seem to suggest that dissecting AAAs in the angiotensin II-infused ApoE $^{-/-}$ mouse model suffer from a similar pathophysiology, this cannot be deduced from the current data. Similarly, any conclusions on human AAA formation would be premature. Moreover, due to the strong competition for PCXTM beam time, and due to the relatively large size and hence long scan time of murine dissecting AAAs, the number of included samples and investigated time points was rather limited. We therefore aim to confirm our findings in a larger sample of angiotensin II-infused ApoE $^{-/-}$ mice, using PCXTM and PCXTM-guided histology to focus on both earlier time points (before any tear or rupture is present) and later time points (after hematoma remodeling). More research is also needed to investigate to what extent our findings have implications on the early stages of human AAA formation and/or vascular dissection.

In conclusion, we demonstrated how PCXTM and PCXTM-guided histology can lead to novel insights in cardiovascular pathology in mice. We visualized macroscopic and microscopic ruptures (both in 2D and 3D) near suprarenal branches in the tunica media of C57BL/6J male mice that were subjected to angiotensin II infusion and systemic neutralization of TGF-β. We demonstrated how these ruptures lead to apparent luminal dilatation and intramural hematoma formation, and provided an explanation for both the observed variability in shape and the predilection for the left suprarenal aorta of angiotensin II-induced dissecting AAAs in mice.

Funding

This research was funded by the Special Research Fund of Ghent University and by internal funds of the Laboratory of Hemodynamics and Cardiovascular Technology, EPFL. . B.T. received a travel grant of the Flemish Fund for Scientific Research, and R.F.A-S. received a grant of the Novartis Consumer Health Foundation.

Acknowledgments

The authors would like to thank Orestis Vardoulis and Iraklis Kourtis for their assistance during the PCXTM scans. Further we wish to acknowledge Agnès Hautier and the entire team of the Histology Core Facility at the Ecole Polytechnique Fédérale de Lausanne (EPFL) for their technical expertise with the PCXTM-guided histology, and dr. José Artacho from the Bioimaging and Optics platform (PTBIOP) at EPFL for his expert help with the image data processing. We also thank Marion Varet and the entire team of the Phenotyping Unit in the Center of PhenoGenomics at the school of Life Sciences in EPFL for their technical and scientific expertise in the micro-CT experiments, dr. Bert Vandeghinste at IBiTech-Medisip at Ghent University for his help with the micro-CT reconstructions, and prof. Julie De Backer at Ghent University and prof. Peter Davies at the University of Pennsylvania for their valuable feedback on the manuscript.

Conflict of Interest

None declared.

References

1. Thompson RW, Geraghty PJ, Lee JK. Abdominal Aortic Aneurysms: Basic Mechanisms and Clinical Implications. *Curr Probl Surg* 2002;**39**:110-230.
2. Lindsay ME, Dietz HC. Lessons on the pathogenesis of aneurysm from heritable conditions. *Nature* 2011;**473**:308-316.
3. Daugherty A, Manning MW, Cassis LA. Angiotensin II promotes atherosclerotic lesions and aneurysms in apolipoprotein E-deficient mice. *J Clin Invest* 2000;**105**:1605-1612.
4. Saraff K, Babamusta F, Cassis LA, Daugherty A. Aortic dissection precedes formation of aneurysms and atherosclerosis in angiotensin II-infused, apolipoprotein E-deficient mice. *Arterioscler Thromb Vasc Biol* 2003;**23**:1621-1626.
5. Manning MW, Cassis LA, Huang J, Szilvassy SJ, Daugherty A. Abdominal aortic aneurysms: fresh insights from a novel animal model of the disease. *Vasc Med* 2002;**7**:45-54.
6. Daugherty A, Cassis LA, Lu H. Complex pathologies of angiotensin II-induced abdominal aortic aneurysms. *J Zhejiang Univ (Agric Life Sci)* 2011;**12**:624-628.
7. Rateri DL, Howatt DA, Moorleghen JJ, Charnigo R, Cassis LA, Daugherty A. Prolonged Infusion of Angiotensin II in apoE−/− Mice Promotes Macrophage Recruitment with Continued Expansion of Abdominal Aortic Aneurysm. *Am J Pathol* 2011;**179**:1542-1548.
8. Wang Y, Ait-Oufella H, Herbin O, Bonnin P, Ramkhelawon B, Taleb S, Huang J, Offenstadt G, Combadiere C, Renia L, Johnson JL, Tharaux P-L, Tedgui A, Mallat Z. TGF-beta activity protects against inflammatory aortic aneurysm progression and complications in angiotensin II-infused mice. *J Clin Invest* 2010;**120**:422-432.
9. Klink A, Heynens J, Herranz B, Lobatto ME, Arias T, Sanders HMHF, Strijkers GJ, Merkx M, Nicolay K, Fuster V, Tedgui A, Mallat Z, Mulder WJM, Fayad ZA. In Vivo Characterization of a New Abdominal Aortic Aneurysm Mouse Model With Conventional and Molecular Magnetic Resonance Imaging. *J Am Coll Cardiol* 2011;**58**:2522-2530.
10. Habashi JP, Doyle JJ, Holm TM, Aziz H, Schoenhoff F, Bedja D, Chen Y, Modiri AN, Judge DP, Dietz HC. Angiotensin II Type 2 Receptor Signaling Attenuates Aortic Aneurysm in Mice Through ERK Antagonism. *Science* 2011;**332**:361-365.
11. Satoh K, Nigro P, Matoba T, O'Dell MR, Cui Z, Shi X, Mohan A, Yan C, Abe J-i, Illig KA, Berk BC. Cyclophilin A enhances vascular oxidative stress and the development of angiotensin II-induced aortic aneurysms. *Nat Med* 2009;**15**:649-656.
12. Daugherty A, Manning MW, Cassis LA. Antagonism of AT2 receptors augments Angiotensin II-induced abdominal aortic aneurysms and atherosclerosis. *Br J Pharmacol* 2001;**134**:865-870.
13. Kristo F, Hardy GJ, Anderson TJT, Sinha S, Ahluwalia N, Lin AY, Passeri J, Scherrer-Crosbie M, Gerszten RE. Pharmacological inhibition of BLT1 diminishes early abdominal aneurysm formation. *Atherosclerosis* 2010;**210**:107-113.
14. Malekzadeh S, Fraga-Silva RA, Trachet B, Montecucco F, Mach F, Stergiopulos N. Role of the renin–angiotensin system on abdominal aortic aneurysms. *Eur J Clin Invest* 2013;**43**:1328-1338.
15. Golledge J, Cullen B, Moran C, Rush C. Efficacy of Simvastatin in Reducing Aortic Dilatation in Mouse Models of Abdominal Aortic Aneurysm. *Cardiovasc Drugs Ther* 2010;**24**:373-378.

16. Michel J-B, Martin-Ventura J-L, Egido J, Sakalihasan N, Treska V, Lindholt J, Allaire E, Thorsteinsdottir U, Cockerill G, Swedenborg J. Novel aspects of the pathogenesis of aneurysms of the abdominal aorta in humans. *Cardiovasc Res* 2011;**90**:18-27.
17. Bruemmer D, Daugherty A, Lu H, Rateri DL. Relevance of angiotensin II-induced aortic pathologies in mice to human aortic aneurysms. *Ann N Y Acad Sci* 2011;**1245**:7-10.
18. Schriefl AJ, Collins MJ, Pierce DM, Holzapfel GA, Niklason LE, Humphrey JD. Remodeling of Intramural Thrombus and Collagen in an Ang-II Infusion ApoE−/− Model of Dissecting Aortic Aneurysms. *Thromb Res* 2012;**130**:e139-e146.
19. Trachet B, Renard M, De Santis G, Staelens S, De Backer J, Antiga L, Loeys B, Segers P. An integrated framework to quantitatively link mouse-specific hemodynamics to aneurysm formation in angiotensin II-infused ApoE -/- mice. *Ann Biomed Eng* 2011;**39**:2430-2444.
20. Goergen CJ, Barr KN, Huynh DT, Eastham-Anderson JR, Choi G, Hedehus M, Dalman RL, Connolly AJ, Taylor CA, Tsao PS, Greve JM. In Vivo Quantification of Murine Aortic Cyclic Strain, Motion, and Curvature: Implications for Abdominal Aortic Aneurysm Growth. *J Magn Reson Imaging* 2010;**32**:847-858.
21. Turner GH, Olzinski AR, Bernard RE, Aravindhan K, Karr HW, Mirabile RC, Willette RN, Gough PJ, Jucker BM. In vivo serial assessment of aortic aneurysm formation in apolipoprotein E-deficient mice via MRI. *Circ Cardiovasc Imaging* 2008;**1**:220-226.
22. Ford MD, Black AT, Cao RY, Funk CD, Piomelli U. Hemodynamics of the Mouse Abdominal Aortic Aneurysm. *J Biomech Eng* 2011;**133**.
23. Stampanoni M, Borchert G, Wyss P, Abela R, Patterson B, Hunt S, Vermeulen D, Rüegsegger P. High resolution X-ray detector for synchrotron-based microtomography. *Nucl Instrum Meth A* 2002;**491**:291-301.
24. McDonald SA, Marone F, Hintermuller C, Mikuljan G, David C, Pfeiffer F, Stampanoni M. Advanced phase-contrast imaging using a grating interferometer. *J Synchrotron Radiat* 2009;**16**:562-572.
25. McGavin MD, Zachary JF. Pathologic Basis of Veterinary Disease, 4th edition. Missouri: Mosby Elsevier, 2007.
26. Feil S, Fehrenbacher B, Lukowski R, Essmann F, Schulze-Osthoff K, Schaller M, Feil R. Transdifferentiation of Vascular Smooth Muscle Cells to Macrophage-Like Cells During Atherogenesis. *Circ Res* 2014.
27. Gavish L, Beeri R, Gilon D, Rubinstein C, Berlatzky Y, Gavish LY, Bulut A, Harlev M, Reissman P, Gertz SD. Inadequate reinforcement of transmedial disruptions at branch points subtends aortic aneurysm formation in apolipoprotein-E-deficient mice. *Cardiovasc Pathol* 2014;**23**:152-159.
28. Peiffer V, Sherwin SJ, Weinberg PD. Computation in the rabbit aorta of a new metric - the transverse wall shear stress - to quantify the multidirectional character of disturbed blood flow. *J Biomech* 2013;**46**:2651-2658.
29. Trachet B, Renard M, Van der Donckt C, Deleye S, Bols J, De Meyer GRY, Staelens S, Loeys BL, Segers P. Longitudinal follow-up of ascending versus abdominal aortic aneurysm formation in angiotensin II-infused ApoE−/− mice. *Artery research* 2014;**8**:16-23.
30. Caro CG. Discovery of the role of wall shear in atherosclerosis. *Arterioscler Thromb Vasc Biol* 2009;**29**:158-161.
31. Kumar V, Abbas AK, Aster JC, Robbins SL, Cotran RS. Robbins and Cotran pathologic basis of disease. 9th edition ed, 2014:495-497

32. Gavish L, Rubinstein C, Berlatzky Y, Gavish LY, Beeri R, Gilon D, Bulut A, Harlev M, Reissman P, Gertz SD. Low level laser arrests abdominal aortic aneurysm by collagen matrix reinforcement in apolipoprotein E-deficient mice. *Lasers Surg Med* 2012;**44**:664-674.
33. Bols J, Degroote J, Trachet B, Verhegghe B, Segers P, Vierendeels J. A computational method to assess the in vivo stresses and unloaded configuration of patient-specific blood vessels. *J Comput Appl Math* 2013;**246**:10-17.
34. Cao RY, Amand T, Ford MD, Piomelli U, Funk CD. The Murine Angiotensin II-Induced Abdominal Aortic Aneurysm Model: Rupture Risk and Inflammatory Progression Patterns. *Front Pharmacol* 2010;**1**:9-9.
35. Sampson UK, Perati PR, Prins PA, Pham W, Liu Z, Harrell FE, Jr., Linton MF, Gore JC, Kon V, Fazio S. Quantitative Estimates of the Variability of In Vivo Sonographic Measurements of the Mouse Aorta for Studies of Abdominal Aortic Aneurysms and Related Arterial Diseases. *J Ultrasound Med* 2011;**30**:773-784.
36. Spin JM, Hsu M, Azuma J, Tedesco MM, Deng A, Dyer JS, Maegdefessel L, Dalman RL, Tsao PS. Transcriptional profiling and network analysis of the murine angiotensin II-induced abdominal aortic aneurysm. *Physiol Genomics* 2011;**43**:993-1003.
37. Gavish L, Rubinstein C, Bulut A, Berlatzky Y, Beeri R, Gilon D, Gavish L, Harlev M, Reissman P, Gertz SD. Low-level laser irradiation inhibits abdominal aortic aneurysm progression in apolipoprotein E-deficient mice. *Cardiovasc Res* 2009;**83**:785-792.
38. Barisione C, Charnigo R, Howatt DA, Moorleghen JJ, Rateri DL, Daugherty A. Rapid dilation of the abdominal aorta during infusion of angiotensin II detected by noninvasive high-frequency ultrasonography. *J Vasc Surg* 2006;**44**:372-376.
39. Prins PA, Hill MF, Airey D, Nwosu S, Perati PR, Tavori H, F. Linton M, Kon V, Fazio S, Sampson UK. Angiotensin-Induced Abdominal Aortic Aneurysms in Hypercholesterolemic Mice: Role of Serum Cholesterol and Temporal Effects of Exposure. *PLoS One* 2014;**9**:e84517.
40. Turner GH, Olzinski AR, Bernard RE, Aravindhan K, Boyle RJ, Newman MJ, Gardner SD, Willette RN, Gough PJ, Jucker BM. Assessment of macrophage infiltration in a Murine model of abdominal aortic aneurysm. *J Magn Reson Imaging* 2009;**30**:455-460.
41. Yao Y, Wang Y, Zhang Y, Li Y, Sheng Z, Wen S, Ma G, Liu N, Fang F, Teng G-J. In Vivo Imaging of Macrophages during the Early-Stages of Abdominal Aortic Aneurysm Using High Resolution MRI in ApoE(-/-) Mice. *PLoS One* 2012;**7**.
42. Fan LM, Douglas G, Bendall JK, McNeill E, Crabtree MJ, Hale AB, Mai A, Li J-M, McAteer MA, Schneider JE, Choudhury RP, Channon KM. Endothelial Cell-Specific ROS Production Increases Susceptibility to Aortic Dissection. *Circulation* 2014.

Figure Abbreviations

R: Right. L: Left. D: Dorsal. V: Ventral. Cau: Caudal. Cra: Cranial.

AA: Abdominal Aorta. FC: False Channel. IH: Intramural Hematoma.

CA: Celiac Artery. MA: Mesenteric Artery. RRA: Right Renal Artery. LRA: Left Renal Artery. IA: Intercostal Artery. SSA: Superior Suprarenal Artery.

Figures

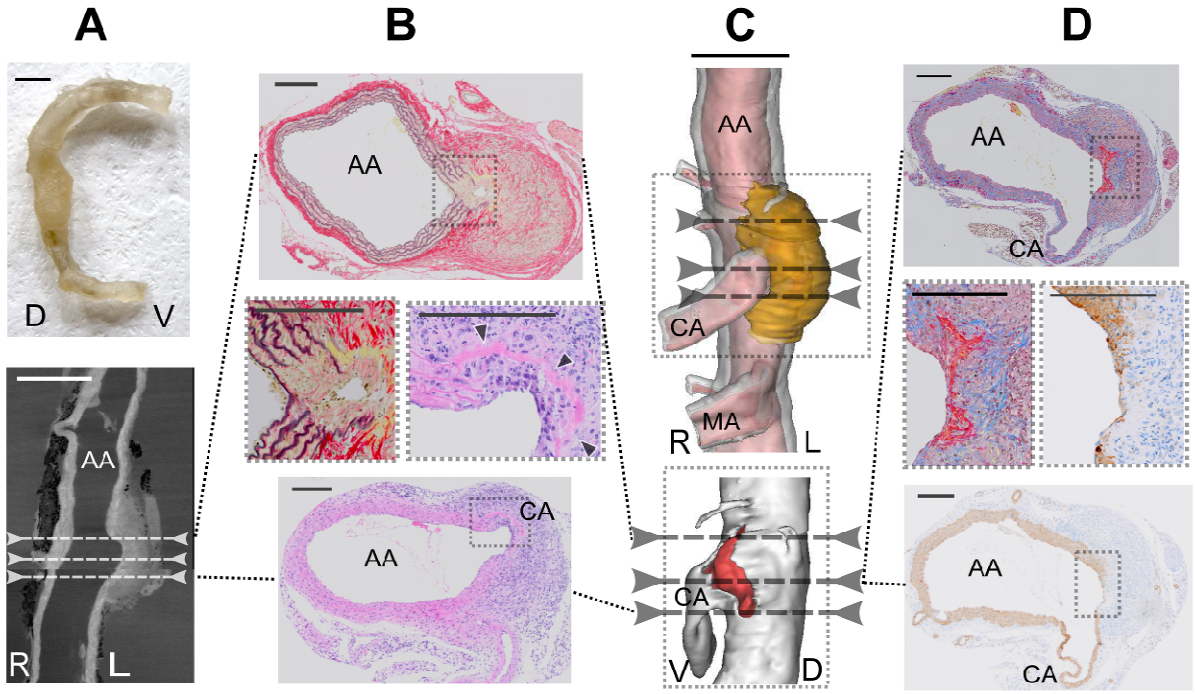

Figure 1. No intramural hematoma, 8 days after first detection on ultrasound. **a.** Top: gross view of the dissecting AAA showing only a small dilation of the wall. Bottom: longitudinal PCXTM. Scale bar represents 1 mm. **b**. PCXTM-guided histology. Top: PCXTM-guided combined Sirius Red (SR) and Miller stain shows destruction of the elastic lamellae and remodeled fibrotic adventitia. Bottom: H&E shows a hemostatic plug covering the tear while the intact adventitia prevents further blood extravasation. Scale bar represents 200 µm. **c.** 3D representation based on PCXTM images. Tunica media in (transparent) white, intramural hematoma in orange, blood filled lumen in (transparent) red. The box shows the tear in the tunica media, on the left side of the celiac artery (tunica media in non-transparent white, blood filled lumen in red, adventitia is hidden). Scale bar represents 1 mm **d.** Top: Martius, Scarlet and Blue (MSB) stain shows the presence of fibrin (in red) within the hemostatic plug. Bottom: smooth muscle α-actin stain shows loss of smooth muscle cells, hence of medial architecture along the tear. Scale bar represents 200 µm.

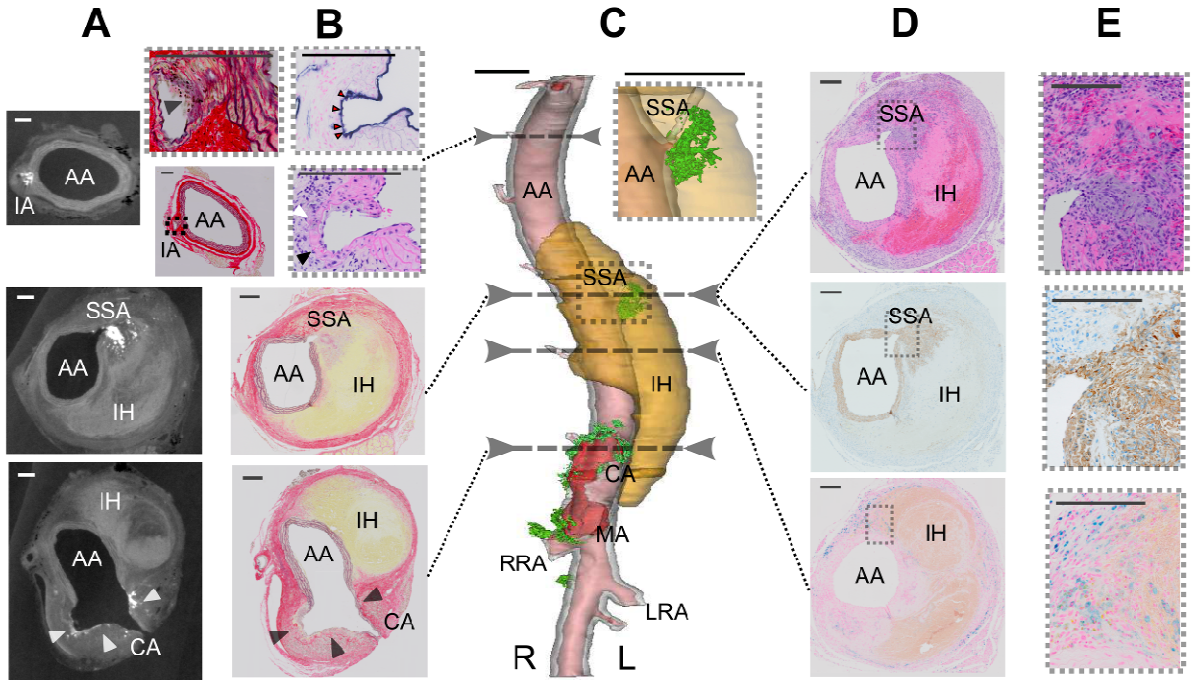

Figure 2. No false channel formation, 9 days after first detection on ultrasound. **a.** Transversal PCXTM images. ExiTron aggregates near the ostium of an intact intercostal artery (top), near the ruptured ostium of the superior suprarenal artery (middle) and at the edges of the tear (indicated by arrowheads) in the tunica media (bottom). Scale bar represents 200 µm. **b.** PCXTM-guided histology. Bottom left: Combined SR and Miller stain at an intercostal artery. The vessel wall at the branch ostium (box, top left) shows loss of normal layered architecure, and numerous cell debris (black arrow). The CD31 stain (box, top right) reveals endothelial cell hypertrophy (red arrowheads), while the H&E stain (box, bottom right) shows microhemorrhages and single erythrocytes (black arrowhead), and cell debris (white arrowhead). Middle: the adventitia (in red) is dissected from the tunica media (in brown) due to an intramural hematoma (in yellow) caused by a rupture at the ostium of the superior suprarenal artery. Bottom: the dissected adventitia does not surround the tear in the tunica media (indicated by arrowheads). Scale bar represents 200 µm. **c.** 3D representation based on PCXTM images. Tunica media in (transparent) white, intramural hematoma in (transparent) orange, blood filled lumen in (transparent) red, ExiTron in green. Leaked ExiTron particles near the ruptured ostium of the superior suprarenal artery (box). The tear in the tunica media is located on the ventral side of the aorta, caudally to the celiac artery. No false channel is formed. Scale bar represents 1 mm. **d, e.** Top: H&E stain shows how hematoma resorption, organization and recanalization start from the luminal edges of the breach proceeding in a centrifugal manner. Middle: smooth muscle α-actin stain shows migrating spindle cells form the lumen into the plug and the hematoma. Bottom: Prussian Blue stain shows hemosiderophages aggregates infiltrating from the outer edges of the hematoma to resorb it. Scale bar represents 200 µm.

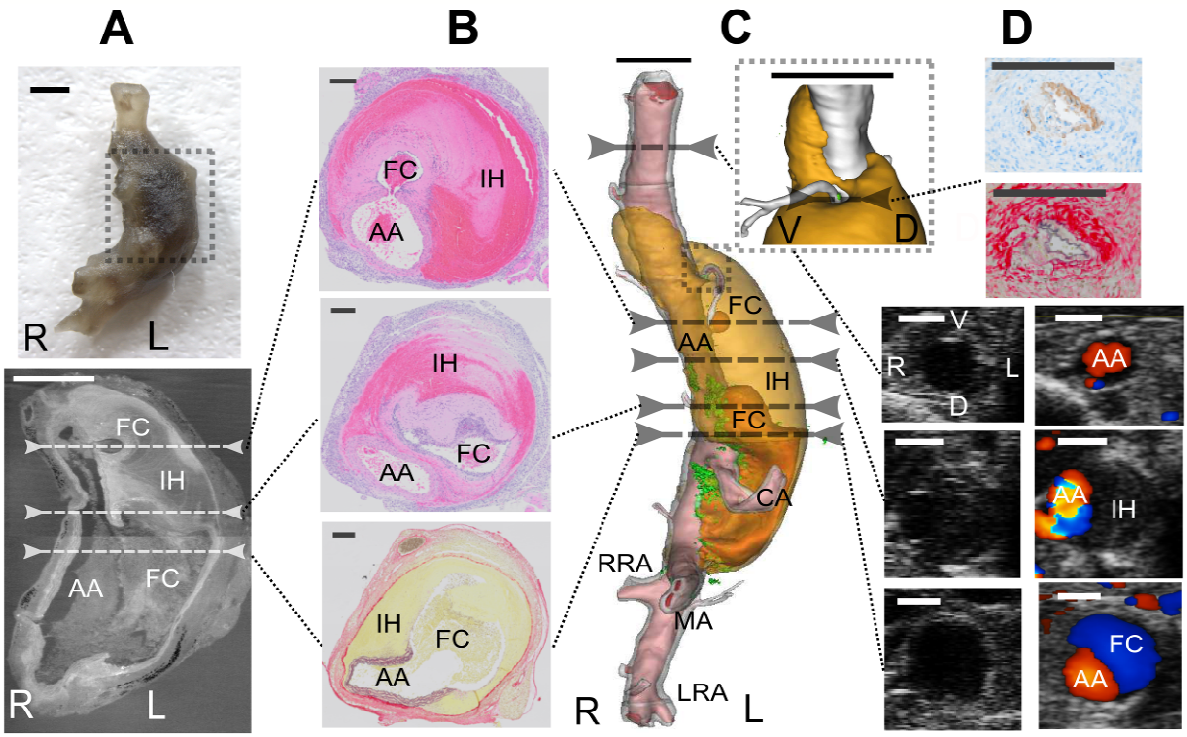

Figure 3. False channel formation, 2 days after first detection on ultrasound. **a**. Top: gross view of the dissecting AAA. Bottom: longitudinal PCXTM. Scale bar represents 1 mm. **b**. PCXTM-guided histology. Top: H&E stain at the ostium of the ruptured superior suprarenal artery. Middle: H&E showing the formation of the false channel into the hematoma. Bottom: combined SR and Miller stain. The hemorrhage caused by the tear in the tunica media is enclosed within the dissected adventitia. Scale bar represents 200 µm. **c.** 3D representation based on PCXTM. Tunica media in (transparent) white, intramural hematoma in (transparent) orange, blood filled lumen in (transparent) red, ExiTron in green. Scale bar represents 1 mm. **d.** Top: the adventitial dissection is prevented to proceed further by a small abdominal branch with mural degeneration at its caudal end, as can be seen on the smooth muscle α-actin and combined SR-Miller stains. Scale bar represents 200 µm. Bottom: BMode (left) and Color Doppler (right) ultrasound. Blood flow towards the transducer in red, away from the transducer in blue. Apparent luminal dilation and retrograde (cranially directed) flow are present at the level of the tear in the tunica media, but not at the intramural hematoma. Scale bar represents 1 mm.

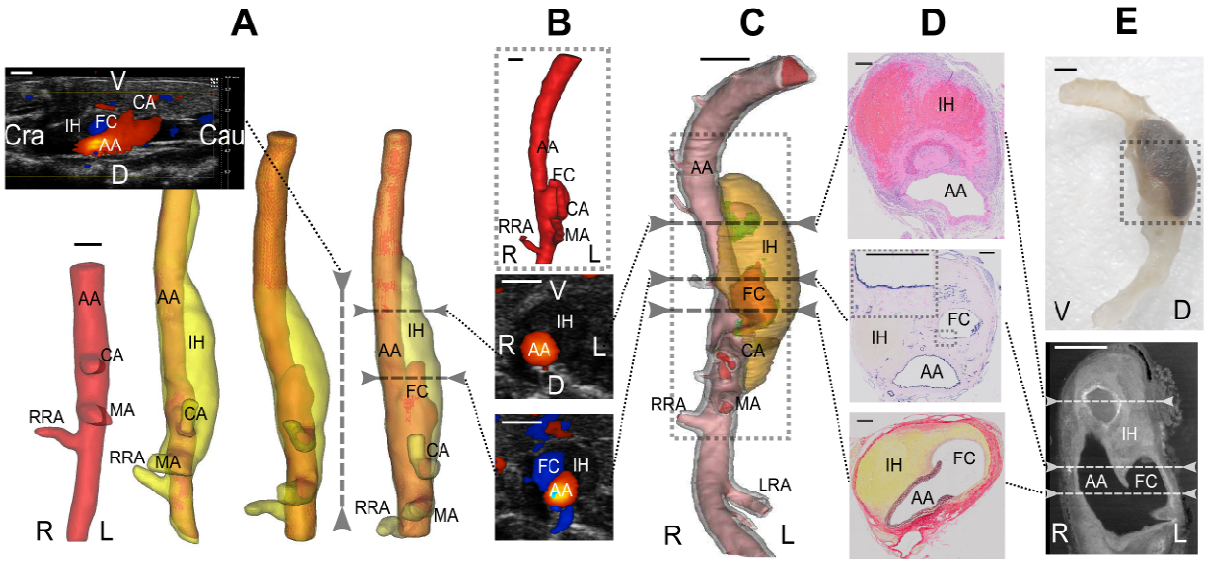

Figure 4. False channel formation, 10 days after first detection on ultrasound. **a.** Modeling of the false channel into the hematoma over time. Reconstructed 3D ultrasound images acquired (from left to right) before dissecting AAA onset and 2, 6 and 10 days after first detection of dissecting AAA. Adventitia in (transparent) yellow and aortic lumen in red. Scale bar represents 1 mm. **b**. Top: micro-CT just before sacrifice. Contrast-enhanced aortic lumen shown in red. Bottom: color Doppler. Blood flow towards the transducer in red, away from the transducer in blue. Retrograde (cranially directed) flow in the false channel. Scale bar represents 1 mm. **c**. 3D representation based on PCXTM images. Tunica media in (transparent) white, intramural hematoma in (transparent) orange, blood filled lumen in (transparent) red, ExiTron in green. The tear in the tunica media is located on the ventral part of the aorta, cranial and caudal to the celiac artery. ExiTron has infiltrated around the rupture site of the superior suprarenal artery. The false channel has protruded cranially into the hematoma. Scale bar represents 1 mm. **d**. PCXTM-guided histology. Top: H&E. The small false lumen at the ostium of the ruptured superior suprarenal artery (Fig. 4*b*, top) has been obliterated by fibrin and platelets deposition, impeding blood flow. Middle: CD-31 shows endothelialization of the false channel by migrating endothelial cells from the breach edges. Bottom: combined SR and Miller stain. The hemorrhage resulting from the tear in the tunica media is enclosed within the dissected adventitia (intramural hematoma). Scale bar represents 200 µm. **e.** Top: gross dissecting AAA. Bottom: longitudinal PCXTM. Scale bar represents 1 mm.

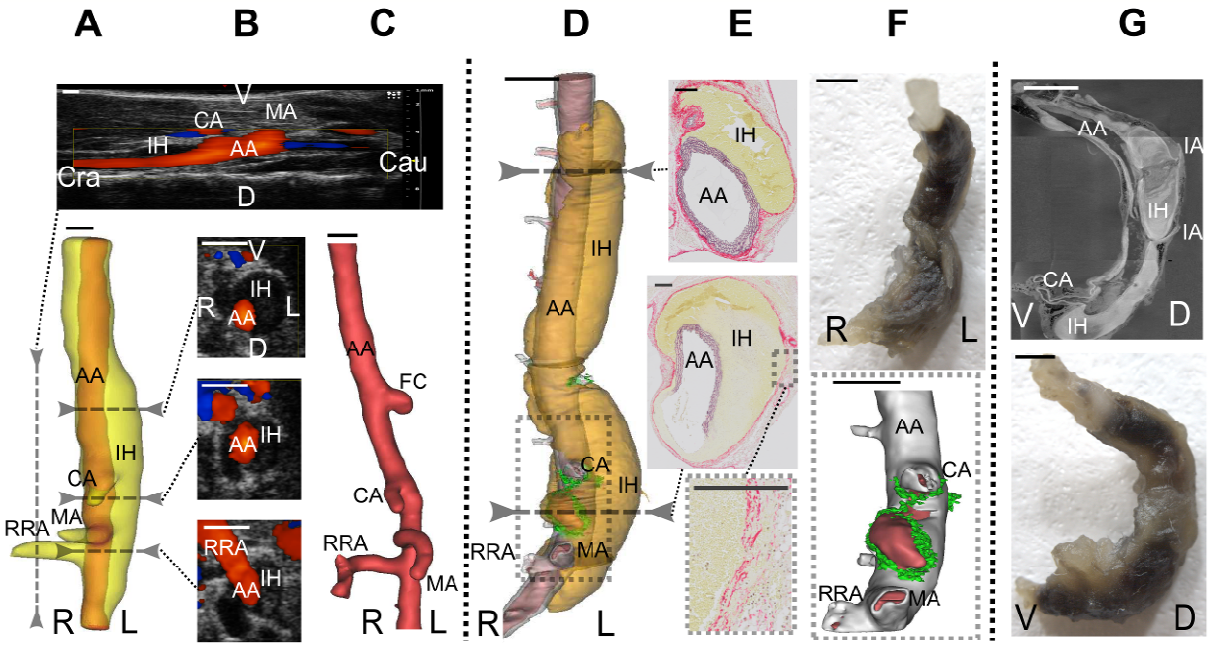

Figure 5. Three dissecting AAAs extending into the thoracic aorta. None of the shown dissecting AAAs was visible on ultrasound 2 days before sacrifice. **a.** 3D ultrasound with remodeled adventitia in (transparent) yellow and lumen in red. Scale bar represents 1 mm. **b**. Color Doppler. None of the imaged locations show blood flow into the hematoma. **c**. Contrast-enhanced micro-CT. No blood flow within the hematoma, except for a small false lumen near the ostium of the superior suprarenal artery. **d**. 3D representation based on PCXTM images. Tunica media in (transparent) white, intramural hematoma in (transparent) orange, blood filled lumen in (transparent) red, ExiTron in green. The tear in the tunica media (panel f, box) is located on the ventral part of the aorta, caudally to the celiac artery. Additional ruptured branches have led to a polymorphic dissecting AAA, with a focal narrowing at the level of the diaphragm. Scale bar represents 1 mm. **e.** combined SR and Miller stains. Top: At the cranial end an intact tunica media lies adjacent to the intramural hematoma that has dissected the tunica adventitia. An intact intercostal artery is visible. Bottom: The tear in the tunica media did not cause a significant dissection of the adventitia compared to the adjacent segment. In the box the adventitia is compressed by the hematoma and separation of collagen fibers, hence rupture of the tunica and further bleeding occur. Scale bar represents 200 µm. **f.** Top: gross dissecting AAA corresponding to the 3D model in panel d. Bottom: zoomed area corresponding to the box in panel d. Scale bar represents 1 mm. **g.** Top: PCXTM image showing the rupture at the caudal part of a dorsal intercostal artery, with concentric flow lines forming around the rupture. The progression of the dissection of the adventitia due to the hemorrhage is stopped by another intercostal artery. Bottom: gross dissecting AAA corresponding to the image on the top panel. Scale bar represents 1 mm.

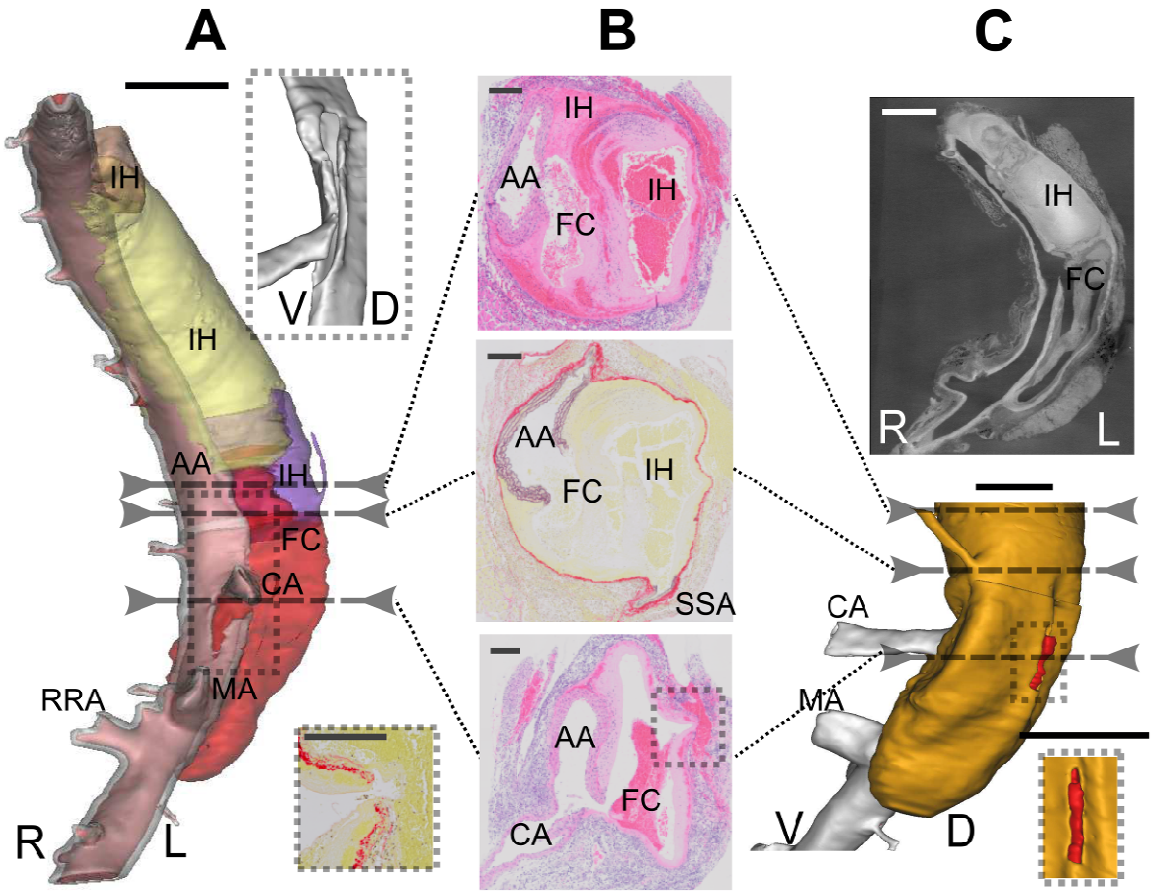

684

685 **Figure 6.** Transmural dissecting AAA rupture. **a**. 3D representation based on PCXTM. Tunica
686 media in (transparent) white, blood filled lumen in (transparent) red, intramural hematomas
687 related to different ruptured branches in (transparent) blue, yellow, brown. Scale bar represents 1
688 mm. **b**. PCXTM-guided histology. Top: H&E. The false channel caused by the tear pushes a
689 second hematoma caused by the ruptured superior suprarenal artery outwards. Middle: Rupture in
690 the elastic lamellae near the ostium of the superior suprarenal artery. Bottom: Multifocal
691 disruption of the adventitia and perivascular soft tissues (box) leads to extravasation of blood into
692 the abdominal cavity (hemoabdomen). Scale bar represents 200 µm. **c**. Top: Longitudinal
693 PCXTM. Bottom: 3D representation based on PCXTM. A tear in the adventitia (shown in
694 orange) can be seen on the dorsal side of the celiac artery (box). Scale bar represents 1 mm.

695

Supplementary material: detailed methods

Animal model. All the procedures were approved by the Ethical Committee of Canton Vaud, Switzerland (EC 2647.1) and performed according to the guidelines from Directive 2010/63/EU of the European Parliament on the protection of animals used for scientific purposes. Male C57BL/6J mice were purchased at the age of 12 weeks from Janvier (Saint Berthevin, France). Water and regular mouse diet were available ad libitum and animals were observed daily after the implantation of pumps. All manipulated mice (n=20) were implanted a 200 µl osmotic pump (model Alzet 2004; Durect Corp, Cupertino, CA), filled with a solution of angiotensin II (Bachem, Bubendorf, Switzerland), on the right flank via an incision in the scapular region. During the implantation mice were anesthetized with 1.5% isoflurane. To avoid interference with the micro-CT images, the metal flow divider inside the pump was replaced by a PEEK alternative (Durect Corp, Cupertino, CA) as previously described [19]. Each pump released angiotensin II over a period of 28 days, at an infusion rate of 1000 ng/kg/min. Systemic neutralization of TGF-β was achieved by intraperitoneal injections of mouse anti–human TGF-β (2G7 clone, 20 mg/kg, three times a week), which resulted in AAA formation in the suprarenal region of the aorta, as previously described [8].

Sample size. 20 manipulated animals and 5 controls were included in the in vivo imaging part of the study. Two animals died of reasons other than transmural aneurysm rupture (found dead in cage without hemoabdomen) and 3 animals did not respond to the treatment and did not develop any aneurysm. The priority criterium for PCXTM imaging was the macroscopic presence of aneurysm after excision. A total of 20 animals (15 dissecting aneurysms, 4 controls and 1 non-responder) were imaged with PCXTM. Since the aim of the study was to describe the morphology of dissecting aneurysms and not to compare a pre-defined effect in different groups, there was no group allocation within the aneurysmatic animals prior to data analysis. There were two experimental groups (dissecting aneurysms and controls) and aneurysmatic animals were classified into different categories a posteriori based on morphological characteristics observed on the PCXTM scans. Subsequently there was no need for randomization of the data or blinding during data analysis.

In vivo imaging. Aneurysm progression was monitored at different time points in vivo using high-frequency ultrasound (Vevo 2100, VisualSonics, Toronto, Canada). A stack of ultrasound images was acquired with a step-motor at an in-plane pixel size of 15 µm and a through-plane slice distance of 32 µm, while abdominal blood flow was visualized by Color Doppler and Pulsed Doppler measurements. Animals were sacrificed between 1 and 14 days after the first detection of aneurysm presence on ultrasound. Before sacrifice, 6 animals with obvious aneurysm presence (as confirmed on ultrasound) were injected intravenously in the lateral tail vein with 4 µl/gram body weight of ExiTron nano 12000 (Miltenyi Biotec, Bergisch Gladbach, Germany). During both ultrasound and micro-CT imaging animals were anesthetized with 1.5% isoflurane. The animals were subsequently scanned in vivo in dorsal recumbency with a Quantum FX micro-CT scanner (Caliper Life Sciences, Hopkinton, Massachusets). Acquisition was performed with a 90 kVp tube voltage and a current of 160 µA. After an in vivo scan time of 2 minutes, images were obtained with a 24 mm transverse field of view and a theoretical spatial pixel size of 50 µm. Micro-CT images were reconstructed using an in-house method based on the iterative maximum-likelihood polychromatic algorithm [43].

At the endpoints of the experiments, the mice were anesthetized by Ketamine/Xylazine (100 mg/kg and 15 mg/kg, respectively) and the sacrifice was resolved following the tissue collection.

PCXTM imaging. After sacrifice, the aorta was flushed in situ by transcardiac perfusion of phosphate buffered saline (PBS, pH 7.4) through the left ventricle. The goal of the perfusion was to wash out erythrocytes from the aortic lumen. The perfusion was performed with a Peri-Star Pro perfusion pump (World Precision Instruments, Sarasota, Florida). As it was performed at the physiological pressure, we do not expect it to influence the aortic or aneurysmatic geometry. In animals that died of transmural aortic rupture, blood had already co-agulated by the time of tissue collection, and flushing was no longer useful. In these animals, the aorta was collected (without flushing) as soon as possible after finding them in the cage. The abdominal aorta of both intact and transmurally ruptured aneurysms was carefully excised and samples were fixed by immersion in 4% paraformaldehyde (PFA) in 0.15 mM PBS. The samples were scanned at the TOMCAT beamline of the Swiss Light Source, Paul Scherrer Institut, Villigen, Switzerland. Per scan 3-4 samples were embedded in 1% agarose gel to stabilize them. The imaging setup consists in two gratings (phase and absorption) with 3.98 and 2 um pitch respectively, positioned at a relative distance of 121 mm. It corresponds to the third fractional Talbot distance at 25 keV. A total of 1441 projections have been acquired over 180 degrees rotations for each of the 5 phase grating steps. The vertical field of view was 4 mm, which required 1h15 minutes of scanning time. Our AAA samples had an average length of 1.2 – 1.6 cm, so each sample required 3-4 stacked scans resulting in a scan time of 4-5 hours.

All reconstructed datasets (in vivo as well as PCXTM) were semi-automatically segmented into 3D models using the commercial software package Mimics (Materialise, Leuven, Belgium).

PCXTM-guided histology. After PCXTM scanning, the samples were fixed as mentioned above, processed and embedded in paraffin according to standard histological procedures. 4 µm thick paraffin sections were carefully compared to the corresponding PCXTM images under a Leica DM750 bright field microscope to spot the exact rupture sites. Selected slides were stained with Haematoxylin-Eosine (H&E) to assess general morphology. Miller stain and Sirius red F3B (CI35782, Direct red 80) were combined to specifically highlight elastic fibers and collagen on the same section. The MSB (Martius, Scarlet and Blue) method was performed to detect fibrin. Prussian Blue, which is a specific stain for iron, confirmed the cytoplasmic hemoglobin and hemosiderin within macrophages (hemosiderophages) at sites of hematoma resorption. Immunohistochemical detection of alpha-smooth muscle actin (α-SMA) was performed using the fully automated Ventana Discovery XT (Roche Diagnostics, Rotkreuz, Switzerland). All steps were performed on the automate with Ventana solutions. Briefly, dewaxed and rehydrated paraffin sections were pretreated with heat using the CC2 solution under standard conditions (36 minutes). The primary antibody mouse anti α-SMA (clone 1A4, Dako) diluted 1:200 in 1% BSA in PBS was incubated 1 hour at 37°C. After incubation with a donkey α-mouse biotin antibody diluted 1:800 in 1% BSA (Jackson ImmunoResearch Laboratories), chromogenic revelation was performed with DabMap kit (Roche Diagnostics, Rotkreuz, Switzerland).

Supplementary material: References

1. Thompson RW, Geraghty PJ, Lee JK. Abdominal Aortic Aneurysms: Basic Mechanisms and Clinical Implications. *Curr Probl Surg* 2002;**39**:110-230.
2. Lindsay ME, Dietz HC. Lessons on the pathogenesis of aneurysm from heritable conditions. *Nature* 2011;**473**:308-316.
3. Daugherty A, Manning MW, Cassis LA. Angiotensin II promotes atherosclerotic lesions and aneurysms in apolipoprotein E-deficient mice. *J Clin Invest* 2000;**105**:1605-1612.
4. Saraff K, Babamusta F, Cassis LA, Daugherty A. Aortic dissection precedes formation of aneurysms and atherosclerosis in angiotensin II-infused, apolipoprotein E-deficient mice. *Arterioscler Thromb Va − c Biol* 2003;**23**:1621-1626.
5. Manning MW, Cassis LA, Huang J, Szilvassy SJ, Daugherty A. Abdominal aortic aneurysms: fresh insights from a novel animal model of the disease. *Vasc Med* 2002;**7**:45-54.
6. Daugherty A, Cassis LA, Lu H. Complex pathologies of angiotensin II-induced abdominal aortic aneurysms. *J Zhejiang Univ (Agric Life Sci)* 2011;**12**:624-628.
7. Rateri DL, Howatt DA, Moorleghen JJ, Charnigo R, Cassis LA, Daugherty A. Prolonged Infusion of Angiotensin II in apoE−/− Mice Promotes Macrophage Recruitment with Continued Expansion of Abdominal Aortic Aneurysm. *Am J Pathol* 2011;**179**:1542-1548.
8. Wang Y, Ait-Oufella H, Herbin O, Bonnin P, Ramkhelawon B, Taleb S, Huang J, Offenstadt G, Combadiere C, Renia L, Johnson JL, Tharaux P-L, Tedgui A, Mallat Z. TGF-beta activity protects against inflammatory aortic aneurysm progression and complications in angiotensin II-infused mice. *J Clin Invest* 2010;**120**:422-432.
9. Klink A, Heynens J, Herranz B, Lobatto ME, Arias T, Sanders HMHF, Strijkers GJ, Merkx M, Nicolay K, Fuster V, Tedgui A, Mallat Z, Mulder WJM, Fayad ZA. In Vivo Characterization of a New Abdominal Aortic Aneurysm Mouse Model With Conventional and Molecular Magnetic Resonance Imaging. *J Am Coll Cardiol* 2011;**58**:2522-2530.
10. Habashi JP, Doyle JJ, Holm TM, Aziz H, Schoenhoff F, Bedja D, Chen Y, Modiri AN, Judge DP, Dietz HC. Angiotensin II Type 2 Receptor Signaling Attenuates Aortic Aneurysm in Mice Through ERK Antagonism. *Science* 2011;**332**:361-365.
11. Satoh K, Nigro P, Matoba T, O'Dell MR, Cui Z, Shi X, Mohan A, Yan C, Abe J-i, Illig KA, Berk BC. Cyclophilin A enhances vascular oxidative stress and the development of angiotensin II-induced aortic aneurysms. *Nat Med* 2009;**15**:649-656.
12. Daugherty A, Manning MW, Cassis LA. Antagonism of AT2 receptors augments Angiotensin II-induced abdominal aortic aneurysms and atherosclerosis. *Br J Pharmacol* 2001;**134**:865-870.
13. Kristo F, Hardy GJ, Anderson TJT, Sinha S, Ahluwalia N, Lin AY, Passeri J, Scherrer-Crosbie M, Gerszten RE. Pharmacological inhibition of BLT1 diminishes early abdominal aneurysm formation. *Atherosclerosis* 2010;**210**:107-113.
14. Malekzadeh S, Fraga-Silva RA, Trachet B, Montecucco F, Mach F, Stergiopulos N. Role of the renin–angiotensin system on abdominal aortic aneurysms. *Eur J Clin Invest* 2013;**43**:1328-1338.
15. Golledge J, Cullen B, Moran C, Rush C. Efficacy of Simvastatin in Reducing Aortic Dilatation in Mouse Models of Abdominal Aortic Aneurysm. *Cardiovasc Drugs Ther* 2010;**24**:373-378.

16. Michel J-B, Martin-Ventura J-L, Egido J, Sakalihasan N, Treska V, Lindholt J, Allaire E, Thorsteinsdottir U, Cockerill G, Swedenborg J. Novel aspects of the pathogenesis of aneurysms of the abdominal aorta in humans. *Cardiovasc Res* 2011;**90**:18-27.
17. Bruemmer D, Daugherty A, Lu H, Rateri DL. Relevance of angiotensin II-induced aortic pathologies in mice to human aortic aneurysms. *Ann N Y Acad Sci* 2011;**1245**:7-10.
18. Schriefl AJ, Collins MJ, Pierce DM, Holzapfel GA, Niklason LE, Humphrey JD. Remodeling of Intramural Thrombus and Collagen in an Ang-II Infusion ApoE−/− Model of Dissecting Aortic Aneurysms. *Thromb Res* 2012;**130**:e139-e146.
19. Trachet B, Renard M, De Santis G, Staelens S, De Backer J, Antiga L, Loeys B, Segers P. An integrated framework to quantitatively link mouse-specific hemodynamics to aneurysm formation in angiotensin II-infused ApoE -/- mice. *Ann Biomed Eng* 2011;**39**:2430-2444.
20. Goergen CJ, Barr KN, Huynh DT, Eastham-Anderson JR, Choi G, Hedehus M, Dalman RL, Connolly AJ, Taylor CA, Tsao PS, Greve JM. In Vivo Quantification of Murine Aortic Cyclic Strain, Motion, and Curvature: Implications for Abdominal Aortic Aneurysm Growth. *J Magn Reson Imaging* 2010;**32**:847-858.
21. Turner GH, Olzinski AR, Bernard RE, Aravindhan K, Karr HW, Mirabile RC, Willette RN, Gough PJ, Jucker BM. In vivo serial assessment of aortic aneurysm formation in apolipoprotein E-deficient mice via MRI. *Circ Cardiovasc Imaging* 2008;**1**:220-226.
22. Ford MD, Black AT, Cao RY, Funk CD, Piomelli U. Hemodynamics of the Mouse Abdominal Aortic Aneurysm. *J Biomech Eng* 2011;**133**.
23. Stampanoni M, Borchert G, Wyss P, Abela R, Patterson B, Hunt S, Vermeulen D, Rüegsegger P. High resolution X-ray detector for synchrotron-based microtomography. *Nucl Instrum Meth A* 2002;**491**:291-301.
24. McDonald SA, Marone F, Hintermuller C, Mikuljan G, David C, Pfeiffer F, Stampanoni M. Advanced phase-contrast imaging using a grating interferometer. *J Synchrotron Radiat* 2009;**16**:562-572.
25. McGavin MD, Zachary JF. Pathologic Basis of Veterinary Disease, 4th edition. Missouri: Mosby Elsevier, 2007.
26. Feil S, Fehrenbacher B, Lukowski R, Essmann F, Schulze-Osthoff K, Schaller M, Feil R. Transdifferentiation of Vascular Smooth Muscle Cells to Macrophage-Like Cells During Atherogenesis. *Circ Res* 2014.
27. Gavish L, Beeri R, Gilon D, Rubinstein C, Berlatzky Y, Gavish LY, Bulut A, Harlev M, Reissman P, Gertz SD. Inadequate reinforcement of transmedial disruptions at branch points subtends aortic aneurysm formation in apolipoprotein-E-deficient mice. *Cardiovasc Pathol* 2014;**23**:152-159.
28. Peiffer V, Sherwin SJ, Weinberg PD. Computation in the rabbit aorta of a new metric - the transverse wall shear stress - to quantify the multidirectional character of disturbed blood flow. *J Biomech* 2013;**46**:2651-2658.
29. Trachet B, Renard M, Van der Donckt C, Deleye S, Bols J, De Meyer GRY, Staelens S, Loeys BL, Segers P. Longitudinal follow-up of ascending versus abdominal aortic aneurysm formation in angiotensin II-infused ApoE−/− mice. *Artery research* 2014;**8**:16-23.
30. Caro CG. Discovery of the role of wall shear in atherosclerosis. *Arterioscler Thromb Va− c Biol* 2009;**29**:158-161.
31. Kumar V, Abbas AK, Aster JC, Robbins SL, Cotran RS. Robbins and Cotran pathologic basis of disease. 9th edition ed, 2014:495-497

32. Gavish L, Rubinstein C, Berlatzky Y, Gavish LY, Beeri R, Gilon D, Bulut A, Harlev M, Reissman P, Gertz SD. Low level laser arrests abdominal aortic aneurysm by collagen matrix reinforcement in apolipoprotein E-deficient mice. *Lasers Surg Med* 2012;**44**:664-674.
33. Bols J, Degroote J, Trachet B, Verhegghe B, Segers P, Vierendeels J. A computational method to assess the in vivo stresses and unloaded configuration of patient-specific blood vessels. *J Comput Appl Math* 2013;**246**:10-17.
34. Cao RY, Amand T, Ford MD, Piomelli U, Funk CD. The Murine Angiotensin II-Induced Abdominal Aortic Aneurysm Model: Rupture Risk and Inflammatory Progression Patterns. *Front Pharmacol* 2010;**1**:9-9.
35. Sampson UK, Perati PR, Prins PA, Pham W, Liu Z, Harrell FE, Jr., Linton MF, Gore JC, Kon V, Fazio S. Quantitative Estimates of the Variability of In Vivo Sonographic Measurements of the Mouse Aorta for Studies of Abdominal Aortic Aneurysms and Related Arterial Diseases. *J Ultrasound Med* 2011;**30**:773-784.
36. Spin JM, Hsu M, Azuma J, Tedesco MM, Deng A, Dyer JS, Maegdefessel L, Dalman RL, Tsao PS. Transcriptional profiling and network analysis of the murine angiotensin II-induced abdominal aortic aneurysm. *Physiol Genomics* 2011;**43**:993-1003.
37. Gavish L, Rubinstein C, Bulut A, Berlatzky Y, Beeri R, Gilon D, Gavish L, Harlev M, Reissman P, Gertz SD. Low-level laser irradiation inhibits abdominal aortic aneurysm progression in apolipoprotein E-deficient mice. *Cardiovasc Res* 2009;**83**:785-792.
38. Barisione C, Charnigo R, Howatt DA, Moorleghen JJ, Rateri DL, Daugherty A. Rapid dilation of the abdominal aorta during infusion of angiotensin II detected by noninvasive high-frequency ultrasonography. *J Vasc Surg* 2006;**44**:372-376.
39. Prins PA, Hill MF, Airey D, Nwosu S, Perati PR, Tavori H, F. Linton M, Kon V, Fazio S, Sampson UK. Angiotensin-Induced Abdominal Aortic Aneurysms in Hypercholesterolemic Mice: Role of Serum Cholesterol and Temporal Effects of Exposure. *PLoS One* 2014;**9**:e84517.
40. Turner GH, Olzinski AR, Bernard RE, Aravindhan K, Boyle RJ, Newman MJ, Gardner SD, Willette RN, Gough PJ, Jucker BM. Assessment of macrophage infiltration in a Murine model of abdominal aortic aneurysm. *J Magn Reson Imaging* 2009;**30**:455-460.
41. Yao Y, Wang Y, Zhang Y, Li Y, Sheng Z, Wen S, Ma G, Liu N, Fang F, Teng G-J. In Vivo Imaging of Macrophages during the Early-Stages of Abdominal Aortic Aneurysm Using High Resolution MRI in ApoE(-/-) Mice. *PLoS One* 2012;**7**.
42. Fan LM, Douglas G, Bendall JK, McNeill E, Crabtree MJ, Hale AB, Mai A, Li J-M, McAteer MA, Schneider JE, Choudhury RP, Channon KM. Endothelial Cell-Specific ROS Production Increases Susceptibility to Aortic Dissection. *Circulation* 2014.
43. De Man B, Nuyts J, Dupont P, Marchal G, Suetens P. An iterative maximum-likelihood polychromatic algorithm for CT. *Medical Imaging, IEEE Transactions on* 2001;**20**:999-1008.